J. Fluid Mech. (2011), *vol.* 676, *pp.* 218–236.
doi:10.1017/jfm.2011.40

Edge pinch instability of oblate liquid metal drops in a transverse AC magnetic field

JĀNIS PRIEDE†

Applied Mathematics Research Centre, Coventry University,
Priory Street, Coventry CV1 5FB, UK

(Received 20 April 2010; revised 20 December 2010; accepted 20 January 2011;
first published online 3 May 2011)

This paper considers the stability of liquid metal drops subject to a high-frequency AC magnetic field. An energy variation principle is derived in terms of the surface integral of the scalar magnetic potential. This principle is applied to a thin perfectly conducting liquid disk, which is used to model the drops constrained in a horizontal gap between two parallel insulating plates. Firstly, the stability of a circular disk is analysed with respect to small-amplitude harmonic edge perturbations. Analytical solution shows that the edge deformations with the azimuthal wavenumbers $m = 2, 3, 4, \ldots$ start to develop as the magnetic Bond number exceeds the critical threshold $Bm_c = 3\pi(m + 1)/2$. The most unstable is $m = 2$ mode, which corresponds to an elliptical deformation. Secondly, strongly deformed equilibrium shapes are modelled numerically by minimising the associated energy in combination with the solution of a surface integral equation for the scalar magnetic potential on an unstructured triangular mesh. The edge instability is found to result in the equilibrium shapes of either two- or threefold rotational symmetry depending on the magnetic field strength and the initial perturbation. The shapes of higher rotational symmetries are unstable and fall back to one of these two basic states. The developed method is both efficient and accurate enough for modelling of strongly deformed drop shapes.

Key words: fingering instability, magnetohydrodynamics, variational methods

1. Introduction

In several metallurgical processes such as, for example, the levitation melting and cold crucible, where the induction heating is used, the surface of liquid metal is subject to AC magnetic field. In such a way, the metal can be not only molten but also evaporated provided that the heating power is high enough (Baptiste *et al.* 2007). Induction heating is accompanied with a pinch effect, which can significantly deform the surface of liquid metal. When a sufficiently strong magnetic field is applied, surface sometimes becomes asymmetric and even strongly irregular (Fautrelle, Sneyd & Etay 2007). This phenomenon is of primary importance for the induction heating of liquid metals because it may have an adverse effect on the heating efficiency and eventually limit the power density the liquid metal can dissipate. Such a surface instability has been observed first by Perrier, Fautrelle & Etay (2003) on a circular layer of Gallium in a mid-frequency AC magnetic field. Analogous instability was studied also by Mohring, Karcher & Schulze (2005) on the free surface of InGaSn

† Email address for correspondence: J.Priede@coventry.ac.uk

melt in the annulus placed under a ring-like circular coil and fed by an alternating current with the frequency in the range of 20–50 kHz. As the current amplitude exceeds a certain critical value, which depends mainly on the annulus width, an initially flat surface acquires a static wavy deformation. At a higher critical current, the deformation rapidly increases and becomes unsteady. In contrast to Perrier *et al.* (2003), who observe only static deformations, Kocourek *et al.* (2006) find a circular sessile drop of InGaSn melt first to squeeze radially with various shape oscillations to set in as the strength of a 20 kHz AC magnetic field is gradually increased. In the former experiment, the surface of liquid metal was exposed to the air and, thus, heavily oxidised that constrained its motion. In the latter experiment, oxidation was prevented by covering the drop by a diluted HCl solution. Later on Conrath, Kocourek & Karcher (2006), Conrath (2007) found static shape deformations when the drop was constrained in a horizontal gap between two parallel plates. Irregular static surface shapes have been observed also by Hinaje, Vinsard & Dufour (2006*a*) on a layer of PbSn alloy covering the bottom of a cylindrical container. The metal layer, which was constrained by the lateral walls of the container and heavily oxidised at the top, broke up revealing the bottom of the container as the strength of a 4 Khz AC magnetic field exceeded a certain critical value. The authors also attempted to model this process numerically using a surface integral equation derived from Green's third identity. This approach, however, is not applicable to thin sheets, for which the double layer contribution vanishes. In a subsequent paper, Hinaje, Vinsard & Dufour (2006*b*) devised a simplified electrotechnical model, which provided a rough estimate of equilibrium shapes. A simple theoretical model for this type of instability was introduced by Priede, Etay & Fautrelle (2006), who analysed the linear stability of the edge of liquid metal layer, which was treated as a perfectly conducting thin liquid sheet in a transverse AC magnetic field. This allowed the authors to determine the wavenumber of the most dangerous perturbation and the critical field strength at which the instability develops in a reasonable agreement with the observations of Mohring *et al.* (2005).

In this paper, an energy variation principle is derived for the equilibrium shapes that develop from the edge pinch instability of flat liquid metal drops, which are modelled as thin perfectly conducting liquid sheets. Firstly, the stability of a circular disk is analysed with respect to small-amplitude harmonic edge perturbations. Analytical solution shows that the edge deformations with the azimuthal wavenumbers $m = 2, 3, 4, \ldots$ start to grow as the magnetic Bond number exceeds the critical threshold $Bm_c = 3\pi(m + 1)/2$. The most unstable is $m = 2$ mode, which corresponds to an elliptical deformation. Secondly, strongly deformed equilibrium shapes are modelled numerically by minimising the associated energy. The electromagnetic problem is formulated in terms of the surface integral equation for the scalar magnetic potential, which is solved numerically on an unstructured triangular mesh covering the surface of the drop. The edge instability is found to result in the equilibrium shapes of either two- ($m = 2$) or threefold ($m = 3$) rotational symmetry depending on the initial perturbation and the magnetic field strength. Although the associated energy of $m = 3$ shapes is higher than that of $m = 2$ ones at the same magnetic field strength, both shapes are separated by a positive energy barrier. This, however, is not the case for equilibrium shapes of higher order symmetries. Although these shapes can be obtained numerically, they turn out to be unstable with respect to small amplitude perturbations of two- or threefold rotational symmetries, which make them fall back to one of the two basic states.

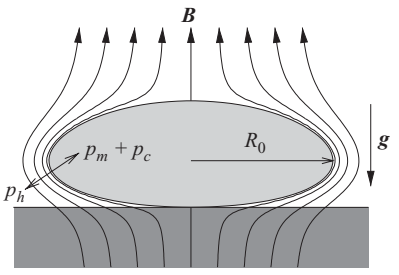

FIGURE 1. Sketch to the formulation of problem.

This paper is organised as follows. In § 2, the problem is formulated and the energy variation principle is derived in terms of the integral of the scalar magnetic potential over the drop surface. This principle is applied in § 3 to obtain an analytical solution for the stability of a circular disk with respect to small-amplitude harmonic edge perturbations. Specific mathematical details of the solution are given in Appendix. In § 4, numerical method is described and validated against the previous analytical solution. Numerical results are presented in § 4. The paper is concluded with a summary and discussion in § 5.

2. Formulation of problem

Consider a drop of liquid metal with the characteristic size R_0, electrical conductivity σ, surface tension γ and density ρ submitted to an AC magnetic field with the spatial amplitude distribution $\boldsymbol{B}(\boldsymbol{r})$, as shown in figure 1. The AC frequency ω is assumed so high that the penetration depth of the magnetic field into the drop $\delta \sim (\mu_0 \sigma \omega)^{-1/2}$, where μ_0 is the vacuum permeability, is negligible with respect to R_0. In this perfect conductor approximation, the magnetic field is tangential to the drop surface S,

$$B_n|_S = 0, \tag{2.1}$$

and the electromagnetic force effectively acts on the surface as the time-averaged magnetic pressure,

$$p_m = \frac{\boldsymbol{B}^2}{4\mu_0}.$$

Equilibrium shape of the drop is determined by the normal stress balance

$$p_h - p_c - p_m|_S = 0, \tag{2.2}$$

where $p_h = \rho \boldsymbol{g} \cdot \boldsymbol{r}$ and $p_c = \gamma \nabla \cdot \boldsymbol{n}$ are the hydrostatic and capillary pressures, respectively, $\boldsymbol{n}$ is the outward surface normal and $\boldsymbol{g}$ is the gravitational acceleration. Multiplying (2.2) by $\boldsymbol{n} \cdot \boldsymbol{\xi}$, where $\boldsymbol{\xi}(\boldsymbol{r})$ is a virtual displacement field conserving the volume, and integrating over S, we obtain

$$W_g + W_s + W_m = 0, \tag{2.3}$$

where $W_g = \rho \int_s (\boldsymbol{g} \cdot \boldsymbol{r}) \boldsymbol{\xi} \cdot \mathrm{d}\boldsymbol{s}$, $W_s = -\gamma \int_s (\nabla \cdot \boldsymbol{n}) \boldsymbol{\xi} \cdot \mathrm{d}\boldsymbol{s}$ and $W_m = -\frac{1}{4\mu_0} \int_s \boldsymbol{B}^2 \boldsymbol{\xi} \cdot \mathrm{d}\boldsymbol{s}$ are the virtual works done by the gravitational, surface tension and magnetic forces, respectively. Since all of these forces, including the magnetic one in the perfect conductor approximation, are conservative, the corresponding works can be expressed as the variations of the associated potential energies. Using the divergence theorem

to change from the surface to volume integrals and taking into account the incompressibility constraint $\nabla\cdot\boldsymbol{\xi}=0$ as well as the Lagrangian variation $\boldsymbol{\xi}\cdot\nabla f=\delta f$, we obtain $W_g=-\delta E_g$, $W_s=-\delta E_s$, and $W_m=-\delta E_m$, where

$$E_g=-\int_V \rho\boldsymbol{g}\cdot\boldsymbol{r}\,\mathrm{d}V, \tag{2.4}$$

$$E_s=\gamma S, \tag{2.5}$$

$$E_m=-\frac{1}{4\mu_0}\int_{\bar V}\boldsymbol{B}^2\mathrm{d}V, \tag{2.6}$$

are the associated potential energies. The minus sign at the last integral is due to the integration over the outer volume $\bar V$. For an equilibrium shape, (2.3) implies $\delta E=0$, where

$$E=E_g+E_s+E_m \tag{2.7}$$

is the total associated energy. This derivation of the energy variation principle appears more straightforward than the original one by Sneyd & Moffatt (1982). Equilibrium shape of the drop corresponds to a stationary point of E, which, as usual, has to be a minimum for the equilibrium to be stable (Chandrasekhar 1961).

2.1. *Magnetic energy in a homogeneous external field*

Further, the external magnetic field $\boldsymbol{B}_e$ is assumed homogeneous, which supposes the drop to be small compared to the inductor generating the field. This allows us to express the magnetic energy (2.6) by an integral over the drop surface as follows. The total magnetic field is a superposition of the external and induced fields $\boldsymbol{B}=\boldsymbol{B}_e+\boldsymbol{B}_i$. Outside the drop, we have $\boldsymbol{B}_i=-\mu_0\nabla\Psi_i$, where Ψ_i is the scalar potential of the induced magnetic field. Then (2.6) can be represented as

$$E_m=E_0+E_1, \tag{2.8}$$

where

$$E_1=-\frac{1}{4\mu_0}\int_{\bar V}\boldsymbol{B}\cdot\boldsymbol{B}_i\,\mathrm{d}V=\frac{1}{4}\int_{S_\infty}\Psi_i\boldsymbol{B}_e\cdot\mathrm{d}\boldsymbol{s}, \tag{2.9}$$

and S_∞ is a remote surface enclosing the drop at $r\to\infty$. The part of the integral over the drop surface S vanishes because of the boundary condition (2.1). Since the induced magnetic field is supposed to fall off at large distances $r\to\infty$ as the dipole field with $\Psi_i\sim 1/r^2$, the last integral converges to a non-zero value. The other contribution to the magnetic energy is

$$E_0=-\frac{1}{4\mu_0}\int_{\bar V}\boldsymbol{B}\cdot\boldsymbol{B}_e\,\mathrm{d}V=-\frac{1}{4\mu_0}\int_{\bar V}\boldsymbol{B}_e^2\,\mathrm{d}V-\frac{1}{4\mu_0}\int_{\bar V}\boldsymbol{B}_i\cdot\boldsymbol{B}_e\,\mathrm{d}V, \tag{2.10}$$

where the first integral represents the energy of the external magnetic field, which is constant, and thus negligible, however, formally it is infinite. Therefore, retaining only the second term in (2.10), we obtain

$$E_0=\frac{1}{4}\int_{\bar V}\nabla\cdot(\boldsymbol{B}_e\Psi_i)\mathrm{d}V=-\frac{1}{4}\int_S\Psi_i\boldsymbol{B}_e\cdot\mathrm{d}\boldsymbol{s}+E_1, \tag{2.11}$$

where the integral is taken over the drop surface S with the outward normal direction. Now it remains to evaluate the integral in (2.9), which is determined by the dipole component of the induced field

$$\Psi_i(\boldsymbol{r})=\frac{1}{4\pi}\frac{\boldsymbol{m}\cdot\boldsymbol{r}}{r^3}, \tag{2.12}$$

where $\boldsymbol{m} = \frac{1}{2}\int_S \boldsymbol{r} \times \boldsymbol{J} \mathrm{d}s$ is the dipole moment of the drop and $\boldsymbol{J}$ is the surface current density. The latter is related to the magnetic field by Ampere's integral current law, which applied to a small surface element results in

$$\boldsymbol{J} = \frac{1}{\mu_0}\, \boldsymbol{n} \times \boldsymbol{B}|_S = \nabla\Psi \times \boldsymbol{n}|_S\,, \tag{2.13}$$

where $\Psi = \Psi_e + \Psi_i$ is the full scalar magnetic potential including also that of homogeneous external field

$$\Psi_e = -\frac{1}{\mu_0}\boldsymbol{r}\cdot\boldsymbol{B}_e. \tag{2.14}$$

Substituting these expressions into (2.9), after some algebra we obtain

$$E_1 = \frac{1}{12}\boldsymbol{B}_e\cdot\boldsymbol{m} = \frac{1}{12}\int_S \Psi\, \boldsymbol{B}_e\cdot \mathrm{d}\boldsymbol{s}. \tag{2.15}$$

The integral above can be represented as

$$E_1 = \frac{1}{12}\left(\int_S \Psi_i \boldsymbol{B}_e\cdot \mathrm{d}\boldsymbol{s} - \frac{V\boldsymbol{B}_e^2}{\mu_0}\right), \tag{2.16}$$

where the second term, which is related to the energy of homogeneous external magnetic inside the drop of fixed volume, is constant and, thus, negligible again. By the same argument, Ψ_i in (2.11) can be substituted by Ψ. Then the magnetic energy (2.8), apart from a constant contribution of the external field, can be written in terms of Ψ as

$$E_m = -\frac{1}{4}\int_S \Psi\, \boldsymbol{B}_e\cdot \mathrm{d}\boldsymbol{s} + 2E_1 = -E_1, \tag{2.17}$$

where E_1 is given by (2.15).

2.2. *Scalar magnetic potential*

There are two alternatives how to find the magnetic potential. First, the solenoidality constraint $\nabla\cdot\boldsymbol{B} = 0$ for a free-space magnetic field $\boldsymbol{B} = -\mu_0\nabla\Psi$ results in

$$\nabla^2\Psi = 0, \tag{2.18}$$

which together with the boundary conditions,

$$\partial_n\Psi|_S = 0, \quad \text{and} \quad \Psi|_{r\to\infty} \to \Psi_e = -\mu_0^{-1}\boldsymbol{r}\cdot\boldsymbol{B}_e, \tag{2.19}$$

governs Ψ outside the drop. This formulation is used in § 3 for analytical treatment of small amplitude deformations of a circular disk by using a singular Taylor-series-type expansion around the basic state. Second, for efficient numerical solution, instead of (2.18), which has to be solved in the whole space outside the drop, it is more advantageous to use Biot–Savart law

$$\boldsymbol{B}(\boldsymbol{r}) = \boldsymbol{B}_0 - \frac{\mu_0}{4\pi}\int_s \frac{\boldsymbol{r}-\boldsymbol{r}'}{|\boldsymbol{r}-\boldsymbol{r}'|^3}\times \boldsymbol{J}(\boldsymbol{r}')\,\mathrm{d}^2\boldsymbol{r}', \tag{2.20}$$

where the prime denotes the integration point. Then the boundary condition (2.1) applied to (2.20) results in the surface integral equation defining Ψ on S

$$\frac{\mu_0}{4\pi}\int_s \frac{\boldsymbol{r}-\boldsymbol{r}'}{|\boldsymbol{r}-\boldsymbol{r}'|^3}\cdot\nabla\Psi(\boldsymbol{r}')\,\mathrm{d}s' = -\boldsymbol{n}\cdot\boldsymbol{B}_e, \tag{2.21}$$

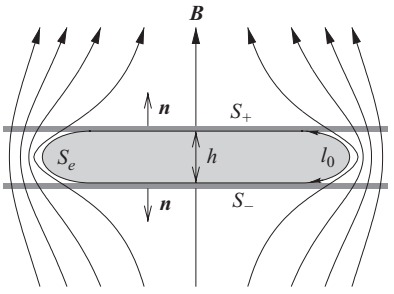

FIGURE 2. A model of liquid layer confined in the gap between two horizontal plates in a transverse AC magnetic field.

which has to be solved for a given shape of the drop to obtain the surface distribution of Ψ, which, in turn, defines the magnetic energy (2.15). Then equilibrium shape is found by minimising the total associated energy (2.7).

2.3. *Thin-drop model*

In the following, we focus on the case of a thin drop confined in a horizontal gap between parallel insulating plates, as shown in figure 2. The drop is modelled by a perfectly conducting liquid sheet with the virtual displacements constrained to the plane of the sheet. The external magnetic field $\boldsymbol{B}_e$ is perpendicular to the sheet. The surface enclosing the sheet consists of the top and bottom parts S_+ and S_-, both with the same area S_0 but opposite normals. Taking into account also that the potential of the induced field changes the sign discontinuously by crossing the sheet, contributions from both surfaces in (2.15) are the same. This results in a factor of 2 at the front of the integrals in (2.15) and (2.21) when the integration is carried out only over the upper part of the sheet. Subsequently, we identify S_0 and Ψ with the top surface and the potential at that surface, respectively. Note that the contribution of the transverse homogeneous field, whose potential (2.14) is constant along the sheet, vanishes in (2.15). For the layer of fixed thickness, gravitational energy is constant and, consequently, irrelevant in the variation of the total energy. Due to the volume conservation and fixed thickness, the horizontal area S_0 is fixed, too. Then the variation of surface is caused only by the stretching of the perimeter $P = \oint_L \mathrm{d}l$, which determines the effective edge area $S_e = Pl_0$ and the corresponding surface energy $E_s = \gamma S_e$, where the arclength l_0 over the edge is assumed to be fixed similar to the layer thickness itself (see figure 2).

Subsequently, all variables are non-dimensionalised by choosing R_0, B_0, R_0B_0 and $\gamma l_0 R_0$ as the length, magnetic field, potential and energy scales, respectively. Then the dimensionless associated energy, which comprises a capillary contribution of the edge and the magnetic energy, can be written as

$$E = \oint_L \mathrm{d}l - \frac{1}{3}Bm \int_S \Psi \,\mathrm{d}s, \tag{2.22}$$

where $Bm = B_0^2 R_0^2/(2\mu_0 \gamma l_0)$ is the magnetic Bond number based on the amplitude of AC magnetic field. Note that there is no difference between the induced and full magnetic field potentials in (2.22) when that of homogeneous field (2.14) is set to be zero along the sheet by a proper choice of additive constant. Actually, this difference is irrelevant because the contribution of homogeneous field in (2.14), as discussed in the previous section, is constant for incompressible liquid. For a flat sheet, (2.21)

takes the following dimensionless form:

$$\frac{1}{2\pi}\int_s \frac{\boldsymbol{r}-\boldsymbol{r}'}{|\boldsymbol{r}-\boldsymbol{r}'|^3}\cdot\nabla\Psi(\boldsymbol{r}')\,\mathrm{d}^2\boldsymbol{r}' = -1. \tag{2.23}$$

For no electric current (2.13) to cross the edge L, $\boldsymbol{\tau}\times\boldsymbol{n}\cdot\boldsymbol{J}|_L = \partial_\tau\Psi|_L = 0$ is required, which implies $\Psi|_L = \text{const}$, where $\boldsymbol{\tau}$ and $\boldsymbol{\tau}\times\boldsymbol{n}$ are the tangent and normal vectors to the edge, respectively, and $\boldsymbol{n}$ is the normal vector to the sheet. As discussed above, we can set

$$\Psi|_L = 0, \tag{2.24}$$

which ensures a zero potential for the homogeneous external field in the plane of the sheet.

3. Analytical solution for the stability of circular disk

Here the approach developed above will be applied to the stability analysis of a circular liquid disk with the radius $R = 1 + R_1 + R_2 + \ldots$, where $R_1 = \hat{R}_1\cos(m\phi)$ is a small perturbation with the amplitude $\hat{R}_1$and the azimuthal wavenumber m, and R_2 is a higher-order small correction to be determined later on. The potential is sought as $\Psi = \Psi_0 + \Psi_1 + \Psi_2 + \ldots$, where

$$\Psi_0(\eta,\xi) = -\frac{2}{\pi}\eta\,[1 + \xi\arctan(\xi)], \tag{3.1}$$

is the potential of circular disk presented in the angular and radial oblate spheroidal coordinates, $0 \leqslant \eta \leqslant 1$ and $0 \leqslant \xi < \infty$ (Li, Kang & Leong 2002), which are related with the cylindrical coordinates by

$$r = \sqrt{(1-\eta^2)(1+\xi^2)}, \tag{3.2}$$

$$z = \eta\xi. \tag{3.3}$$

Note that $\xi = 0$ corresponds to the plane of the disk $z = 0$, where $r = \sqrt{1-\eta^2}$ with $\eta = 0$ corresponding to the edge of a circular disk at $r = 1$. The first-order perturbation of the potential vanishing away from the disk and satisfying the edge condition (2.24), which takes the form

$$\Psi_1|_{r\to 1} = -R_1\left.\frac{\partial\Psi_0}{\partial r}\right|_{r\to 1} = -\frac{2}{\pi}\left.R_1\eta^{-1}\right|_{\eta\to 0}, \tag{3.4}$$

can be written as

$$\Psi_1(\boldsymbol{r}) = R_1\hat{\Psi}_1^m(\eta,\xi), \tag{3.5}$$

where

$$\hat{\Psi}_1^m(\eta,\xi) = -\frac{2}{\pi}\left(\frac{1-\eta^2}{1+\xi^2}\right)^{m/2}\frac{\eta}{\eta^2+\xi^2}. \tag{3.6}$$

The details of the solution above, which apart from slightly different notations are similar to those in Priede *et al.* 2006, can be found in Appendix. Since the energy variation about the equilibrium state is expected to be quadratic in R_1, we need to consider also the next-order radius perturbation R_2, which results from the area conservation $S = \int_{2\pi}\int_0^R r\,\mathrm{d}r\,\mathrm{d}\phi = \pi(1 + \hat{R}_1^2/2 + 2R_2 + \cdots)$ as

$$R_2 = -\hat{R}_1^2/4. \tag{3.7}$$

The second-order potential perturbation, for which the edge condition (2.24) takes the form

$$\Psi_2|_{r\to 1} = -R_1\frac{\partial\Psi_1}{\partial r} - R_2\frac{\partial\Psi_0}{\partial r} - \frac{R_1^2}{2}\frac{\partial^2\Psi_0}{\partial r^2}\bigg|_{r\to 1} = \frac{2}{\pi}R_2(1+\cos(2m\phi))\,(m\eta^{-1}+\eta^{-3})\big|_{\eta\to 0}, \tag{3.8}$$

can be written as $\Psi_2(\eta,\xi) = R_2(\hat{\Psi}_2^0(\eta,\xi) + \hat{\Psi}_2^{2m}(\eta,\xi)\cos(2m\phi))$. Subsequently, we will need only the first term of this expression

$$\hat{\Psi}_2^0(\eta,\xi) = m\hat{\Psi}_1^0(\eta,\xi) + \hat{\Psi}_3^0(\eta,\xi), \tag{3.9}$$

which satisfies (A 1) with $m=0$, where $\hat{\Psi}_1^0(\eta,\xi)$ is defined by (3.6). The second term above is obtained similarly to the first one by applying ∂_z^2 to (3.1), as described in the last paragraph of Appendix, which yields

$$\hat{\Psi}_3^0(\eta,\xi) = -\frac{2}{\pi}\frac{\eta[\eta^2-\xi^2(\xi^2+3(1-\eta^2))]}{(\eta^2+\xi^2)^3}. \tag{3.10}$$

At the disk surface, we have

$$\Psi_0(r) = -\frac{2}{\pi}\sqrt{1-r^2}, \tag{3.11}$$

$$\hat{\Psi}_1^m(r) = -\frac{2}{\pi}\frac{r^m}{\sqrt{1-r^2}}, \tag{3.12}$$

$$\hat{\Psi}_2^0(r) = -\frac{2}{\pi}\frac{m+(1-r^2)^{-1}}{\sqrt{1-r^2}}. \tag{3.13}$$

It is important to note that (3.12) and (3.13) are singular at $r=1$, which is the edge of the unperturbed disk. At the same time, the edge condition (2.24) implies the potential to be regular (zero) at the actual edge of the deformed disk. This implies that the solution above can be regularised by representing it in the radial coordinate $\tilde{r}$ stretched with the radius of the deformed disk. Using the substitution

$$r = R\tilde{r} = (1+\tilde{R})\tilde{r}, \tag{3.14}$$

where $\tilde{R} = R_1 + R_2 + \cdots$ is the radius perturbation, and expanding the solution in power series of $\tilde{R}$ up to the second order in R_1, we obtain a solution of the same asymptotic accuracy, which is free of edge singularities

$$\Psi(r,\phi) = \Psi(\tilde{r}(1+\tilde{R}),\phi) \approx \Psi(\tilde{r},\phi) + \tilde{R}\tilde{r}\frac{\partial\Psi}{\partial\tilde{r}} + \frac{(\tilde{R}\tilde{r})^2}{2}\frac{\partial^2\Psi}{\partial\tilde{r}^2} + \cdots = \tilde{\Psi}(\tilde{r},\phi), \tag{3.15}$$

where $\tilde{\Psi}(r,\phi) = \Psi_0(r) + R_1\tilde{\Psi}_1^m(r) + R_2(\tilde{\Psi}_2^0(r) + \tilde{\Psi}_2^{2m}(r)\cos(2m\phi)) + \cdots$ and

$$\tilde{\Psi}_1^m(r) = -\frac{2}{\pi}\frac{r^m - r^2}{\sqrt{1-r^2}}, \tag{3.16}$$

$$\tilde{\Psi}_2^0(r) = -\frac{2}{\pi}\left[\frac{(m-1)(1-2r^m)-r^2}{\sqrt{1-r^2}} - \frac{2(r^m-1)}{(1-r^2)^{3/2}}\right]. \tag{3.17}$$

Then the magnetic energy term in (2.22) can be evaluated up the first order in R_2 as

$$\int_0^{2\pi}\int_0^R \Psi(r,\phi)r\,\mathrm{d}r\,\mathrm{d}\phi = \int_0^{2\pi} R^2\int_0^1 \tilde{\Psi}(\tilde{r},\phi)\tilde{r}\,\mathrm{d}\tilde{r}\,\mathrm{d}\phi \approx -\bar{E}_m - R_2\tilde{E}_m, \tag{3.18}$$

where $\bar{E}_m$ and $R_2\tilde{E}_m$ are the magnetic energies of circular disk and its leading-order perturbation defined by

$$\bar{E}_m = -2\pi \int_0^1 \Psi_0(r) r \, \mathrm{d}r = \frac{4}{3}, \tag{3.19}$$

$$\tilde{E}_m = -2\pi \int_0^1 \left[\tilde{\Psi}_2^0(r) - 4\tilde{\Psi}_1^m(r)\right] r \, \mathrm{d}r = 4(m-1). \tag{3.20}$$

The surface energy term in (2.22) is evaluated as

$$\oint_L \mathrm{d}l \approx 2\pi(1 - R_2(m^2-1)) = \bar{E}_s + R_2\tilde{E}_s. \tag{3.21}$$

Then the total energy variation is

$$\delta E = \frac{1}{2} R_2(\tilde{E}_s + \tilde{E}_m) = -R_2(m-1)\left(\pi(m+1) - \frac{2}{3}Bm\right). \tag{3.22}$$

Note that there is no energy variation for $m = 1$ mode, which corresponds to the shift of the disk as whole. Circular disk is stable with respect to small perturbation with $m > 1$ as long as its energy is at minimum, i.e. $\delta E > 0$. Since according to (3.7) $R_2 < 0$, the stability condition for $m = 2, 3, \ldots$ is satisfied as long as

$$Bm \leqslant 3(m+1)\pi/2. \tag{3.23}$$

The first unstable mode with $m = 2$, which corresponds to an elliptical deformation, appears as Bm exceeds the critical value

$$Bm_c = \frac{9}{2}\pi. \tag{3.24}$$

This critical value is by a factor of 3 greater than the one found by our previous linear stability analysis (Priede, Etay & Fautrelle 2006). The cause of this discrepancy is discussed in the conclusion of the paper.

4. Numerical solution

This section introduces the numerical method which will be used subsequently to find equilibrium shapes of thin drops by the approach described in § 2. Numerical solution will also be verified against the analytical results obtained in the previous section. To solve (2.23) with the edge condition (2.24), which define Ψ over the drop surface S, the latter is tiled into triangular elements as shown in figure 3(*a*). Triangulation is carried out as follows. Firstly, we take a regular hexagon inscribed in the unit circle and tile it using equilateral triangles with the side length $1/N$. Secondly, the hexagon is stretched radially to fit the unit circle. Then six points are discarded from the perimeter and the remaining $6(N-1)$ points are redistributed uniformly against the midpoints of the previous radial level. This produces a more regular triangulation at the edge, which yields a slightly higher numerical accuracy. As a result, we obtain a triangular mesh with $6N^2-6$ elements and $3N\times(N+1)-5$ vertices. Following the finite element approach, Ψ is sought at the vertices and interpolated linearly within the elements. To determine Ψ at the vertices, we need a corresponding number of equations, which are obtained by numerically approximating (2.23) at the inner points and applying the edge condition (2.24) at the peripheral points. The integral in (2.23) is represented as a sum of integrals over separate elements, which

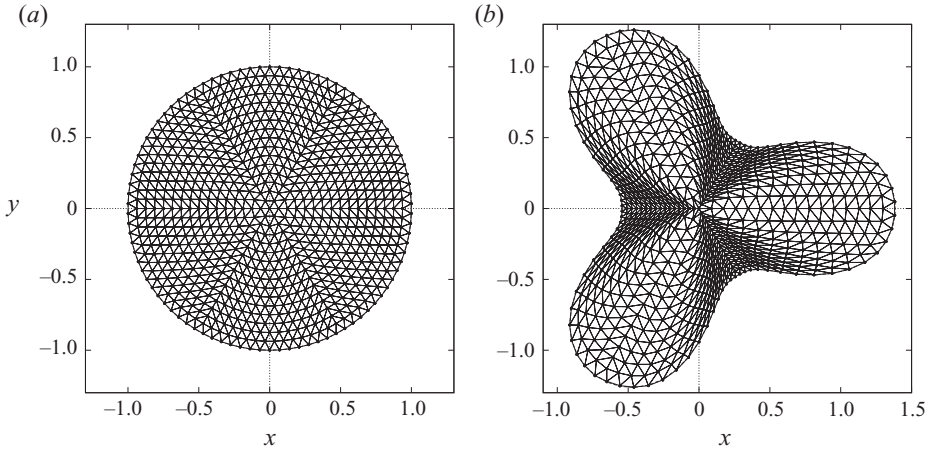

FIGURE 3. Triangulation of the unit circle with $N = 16$ elements along the radius (a) and a radially stretched mesh fitting the drop shape (b).

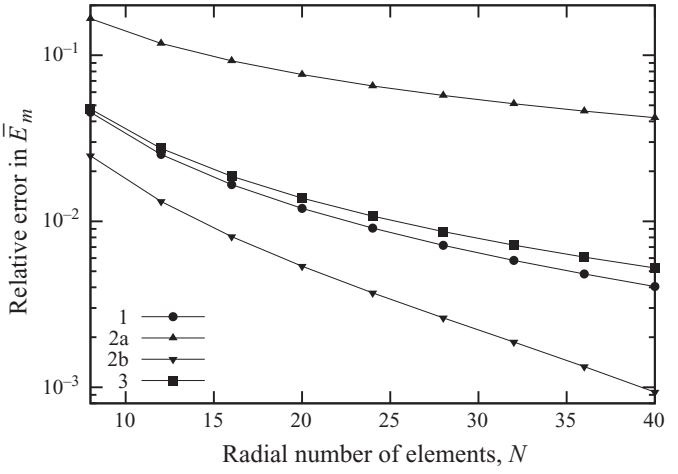

FIGURE 4. The relative error in the magnetic energy of circular disk (3.19) against the radial number of elements N for four different Gaussian quadratures: (1) linear quadrature using only the centre point with the weight factor 1; (2a) and (2b) quadratic quadratures using three symmetric points with the barycentric coordinates $(2/3, 1/6, 1/6)$ and $(1/2, 1/2, 0)$, respectively, and the weight factors 1/3; (3) four-point cubic quadrature using the centre point with the weight factor $-27/48$ and three symmetric points with the barycentric coordinates $(3/5, 1/5, 1/5)$ and weight factors 25/48 (Cowper 1973).

are approximated by the Gaussian quadratures for triangles. Thus, for a given mesh $\boldsymbol{r}_i = (x_i, y_i)$, we obtain a system of linear equations with a dense matrix for unknown $\Psi_i = \Psi(\boldsymbol{r}_i)$, which are found by the LU decomposition method.

The convergence of the magnetic energy for circular disk, $\bar{E}_m$ defined by (3.19), is shown in figure 4 against the radial number of elements N for four different quadratures. Accuracy is lower for the Gaussian quadratures with the evaluation points located closer to the mesh points. This is because of the integrand singularities encountered when the observation point belongs to the element over which the integral is evaluated. Subsequently, we use a quadratic quadrature with three evaluation points

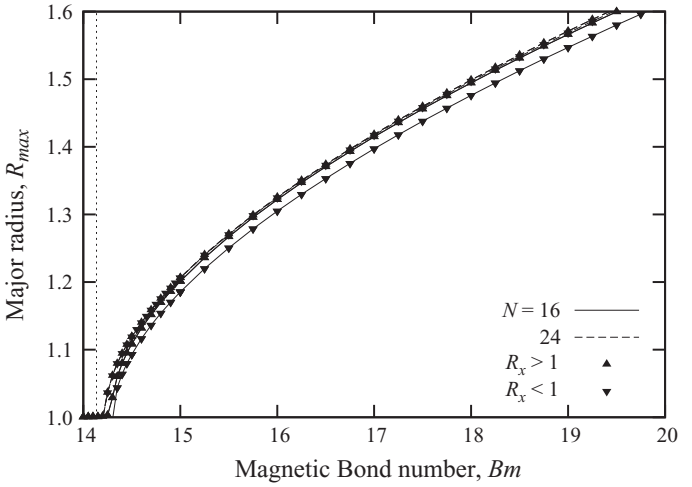

FIGURE 5. Major radius $R_{max} = \max(R_x, 1/R_x)$ versus the magnetic Bond number Bm for both stretched ($R_x > 1$) and squeezed ($R_x < 1$) along the x-axis ellipses with $N = 16, 24$ elements in the radial direction. The vertical dashed line shows the theoretical threshold value (3.24).

located at the side midpoints of the element (curve 2b in figure 4), which provides the highest accuracy. For the linear elements used here, the integral in (2.23) can, in principle, be evaluated exactly. However, such an approach is not applicable because the singularities between adjacent elements do not cancel out when the current distribution is a piece-wise constant, as in this case, rather than continuous. Nevertheless, Gaussian quadratures still provide a reasonably accurate result also in this case.

To verify the analytical solution obtained in the previous section, we first restrict the drop shape to an ellipse defined parametrically by the mesh point coordinates

$$\boldsymbol{r}_i = (x_i^0 R_x, y_i^0/R_x), \tag{4.1}$$

where $(x_i^0, y_i^0) = \boldsymbol{r}_i^0$ are the mesh points for a circular disk and R_x is a parameter defining the x-radius of ellipse. For a given Bm, equilibrium shape is found by using a Powell-type algorithm (Press, Teukolsky & Vetterling 1996) to minimise the associated energy (2.22) with respect to R_x. For each R_x, firstly, Ψ_i is found by solving the system of linear equations for the corresponding distribution of mesh points (4.1). Secondly, integrals in (2.22) are evaluated numerically for the given distributions of $\boldsymbol{r}_i$ and Ψ_i.

As seen in figure 5, which shows the major radius of ellipse versus Bm, the critical value of Bm, by exceeding which the drop starts to deform, is slightly above its theoretical value (3.24). For $N = 16$ elements in the radial direction, the major radius slightly varies depending on whether the ellipse is stretched ($R_x > 1$) or squeezed ($R_x < 1$) along the x-axis. Although these two cases differ only by the orientation of the major axis of ellipse along the x- or y-axis, which are both theoretically equivalent, this small difference is due to the sixfold rotational symmetry of the mesh, which is invariant upon rotation by 60° but not by 90°. For $N = 24$, no difference is noticeable between the $R_x > 1$ and $R_x < 1$ cases.

Subsequently, we search for the disk radius in the following area-conserving form:

$$R^2(\phi) = 1 + \sum_{m=2}^{M+1} [R_m^c \cos(m\phi) + R_m^s \sin(m\phi)], \tag{4.2}$$

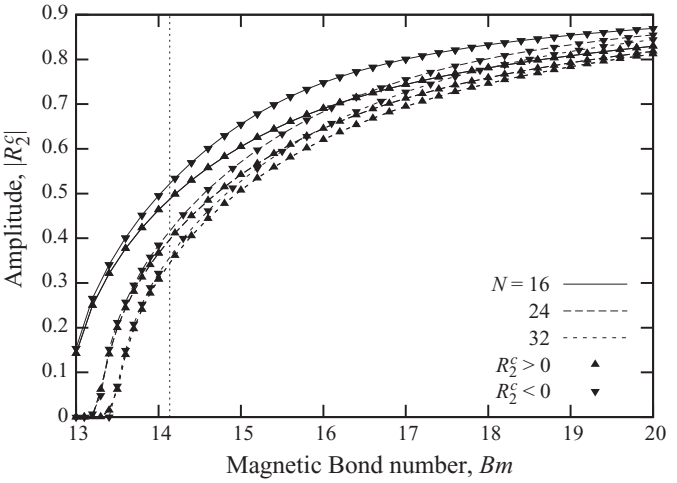

FIGURE 6. Amplitude R_2^c of the radius perturbation versus the magnetic Bond number Bm for the drops squeezed along either the y-axis ($R_2^c > 0$) or the x-axis ($R_2^c < 0$) with $N = 16, 24, 32$ elements in the radial direction. The vertical dashed line shows the theoretical threshold value (3.24).

where R_m^c and R_m^s are unknown amplitudes of cosine and sine terms in the Fourier series expansion of $R^2(\phi)$. Due to the area conservation and the mass centre fixed at the origin, (4.2) does not contain $m = 0$ and $m = 1$ terms. Moreover, owing to the rotational invariance, we can set $R_2^s = 0$, which fixes the orientation of the drop up to a rotation by 90° provided that $R_2^c \neq 0$. This leaves $2M - 1$ unknown coefficients in (4.2) for the minimisation of the associated energy (2.22). The number of azimuthal modes M is chosen to ensure the convergence of equilibrium shapes. In this case, the mesh of unit circle is deformed radially to fit the disk

$$(r_i, \phi_i) = (r_i^0 R(\phi_i^0), \phi_i^0), \tag{4.3}$$

where (r_i^0, ϕ_i^0) and (r_i, ϕ_i) are the polar coordinates of the mesh points for circular and deformed disks, respectively.

For comparison with the case of ellipse considered above, we start with $M = 1$, which leaves only one coefficient, R_2^c, in (4.2) to be determined. As seen in figure 6, which shows R_2^c versus Bm for three numerical resolutions and two perpendicular orientations of the drop determined by the sign of R_2^c, the radial deformation of the mesh (4.3) results in a reduced numerical accuracy of the critical value of Bm, which for $N = 24$ elements in the radial direction is about 6% lower than its theoretical value (3.24). There is also a small difference in the shape depending on whether the drop is squeezed along the y- or x-axis (see figure 7a). Figures 7(a) and 7(b) show that the shape changes very little as the number of azimuthal modes and that of the elements in radial direction reach $M = 15$ and $N = 24$, respectively. In the following, we will be using these values unless stated otherwise.

The equilibrium shapes found as the magnetic field is gradually increased are shown in figure 8(a). At $Bm_c \approx 13.6$, which due to the numerical approximation is slightly below the theoretically predicted stability threshold (3.24), the drop turns noticeably elliptic and rapidly elongates with a further increase in Bm. For $Bm \gtrsim 15$, the drop starts to tighten around the middle part. No equilibrium shapes of this type can be found for $Bm \gtrsim 25$. This implies that the drop may split up into two as the narrowing

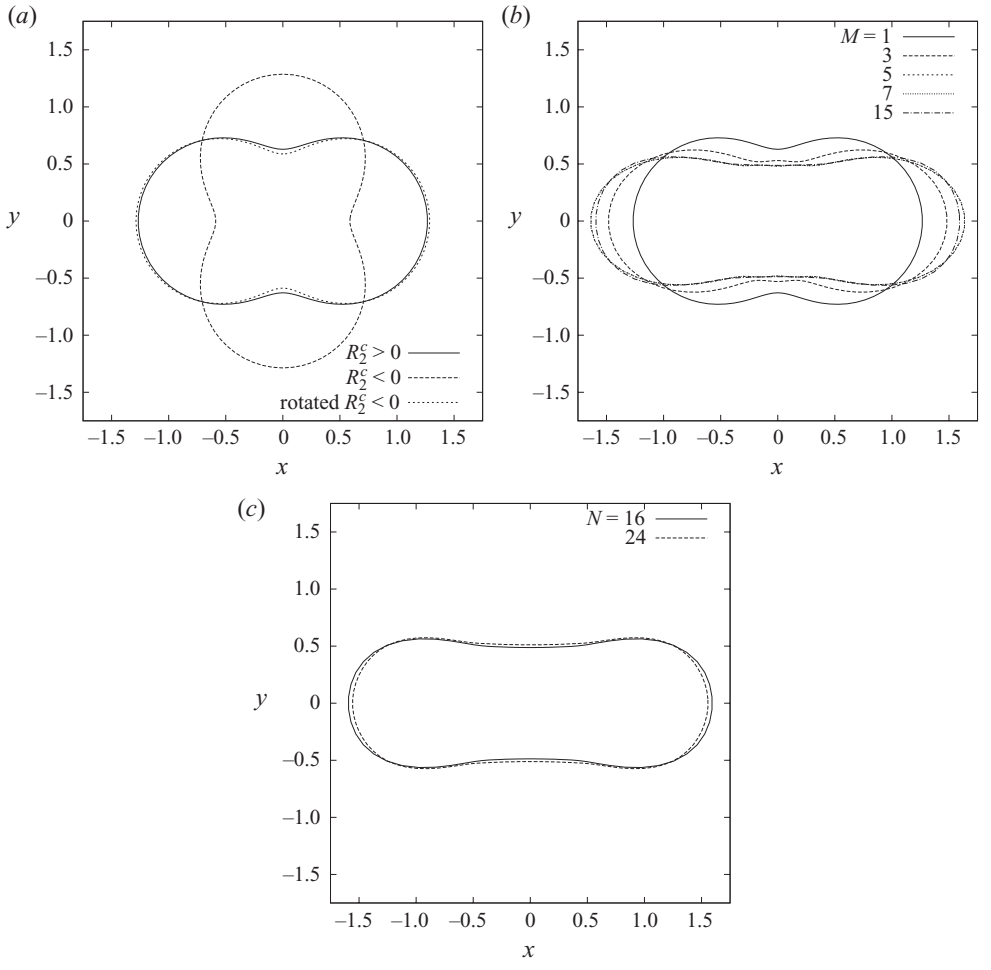

FIGURE 7. Equilibrium shapes at $Bm = 15$ found with one azimuthal mode ($M = 1$) and $N = 16$ elements in radial direction for the disks squeezed along the y- and x-axes, which correspond to $R_2^c > 0$ and $R_2^c < 0$, respectively (a), $M = 1, 3, 5, 7, 15$ and $N = 16$ for $R_2^c > 0$ (b), $M = 15$ with $N = 16, 24$ for $R_2^c > 0$ (c).

of the middle reaches a certain critical value. The splitting of the drop is not captured by this numerical method, which breaks down as the neck between two parts of the drop becomes too thin.

Alternatively, when the magnetic field is applied instantly with $Bm \approx 20$ to a drop with some initial $m = 3$ perturbation, equilibrium shapes with a threefold rotational symmetry shown in figure 8(b) are obtained. As seen in figure 9, the associated energy of $m = 3$ mode is higher than that of $m = 2$ mode, which is also possible at the same Bm. Nevertheless, the shapes with threefold symmetry are stable because they are separated from the twofold symmetry shapes by a finite energy barrier.

This, however, is not the case for the $m = 4$ and $m = 5$ symmetry shapes shown in figures 10(a) and 10(b), which can be obtained only when the corresponding symmetry is explicitly imposed in series (4.2) by ignoring all other modes. As seen in figure 11, the associated energy of four- and fivefold symmetries, in contrast to that of two- and threefold symmetries, decreases upon $m = 2$ and $m = 3$ radius perturbations. This

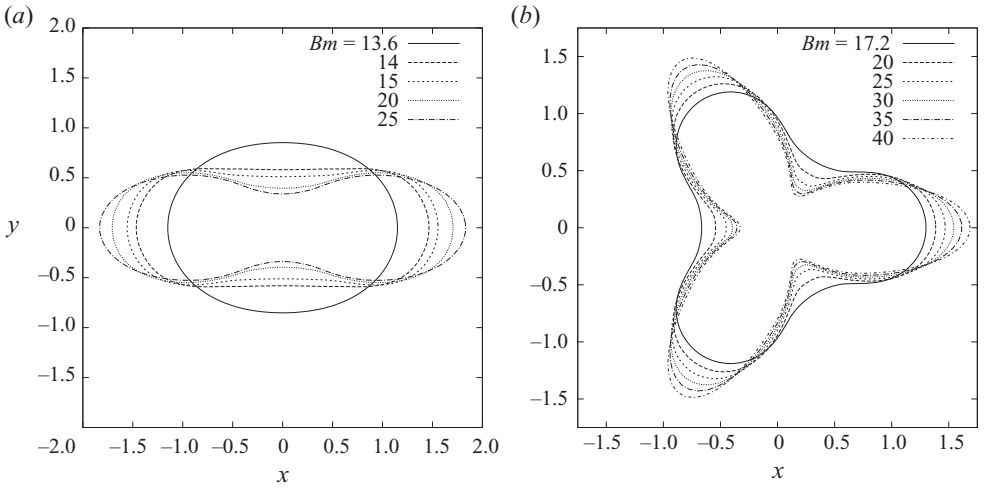

FIGURE 8. Equilibrium shapes for symmetries $m = 2$ (a) and $m = 3$ (b) at various magnetic Bond numbers.

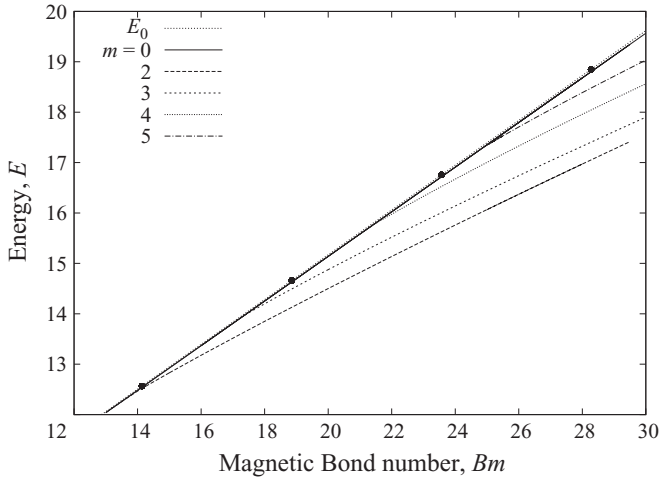

FIGURE 9. The associated energy (2.22) versus Bm for the shapes of various rotational symmetries. $E_0 = 2\pi + \frac{4}{9}Bm$ is the associated energy of circular disk. The dots show the analytical bifurcation points (3.23).

implies that four- and fivefold symmetry shapes are indeed unstable with respect to these perturbations.

5. Summary and conclusions

In this study, we have numerically modelled strongly deformed equilibrium shapes of a flat liquid metal drop subject to a transverse high-frequency AC magnetic field. The drop was treated as a thin liquid layer confined in a horizontal gap between two parallel insulating plates. AC frequency was assumed high so that the magnetic field was effectively expelled from the drop by the skin effect. Equilibrium shapes of the drop were found by using a variational principle for the associated energy involving the surface and magnetic contributions. Using Biot–Savart law,

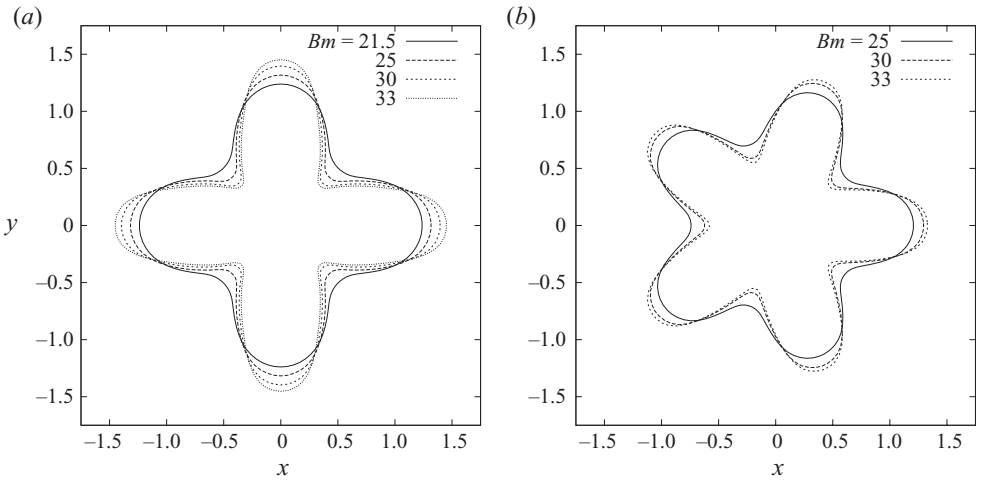

FIGURE 10. Equilibrium shapes for symmetries $m=4$ (a) and $m=5$ (b) at various magnetic Bond numbers.

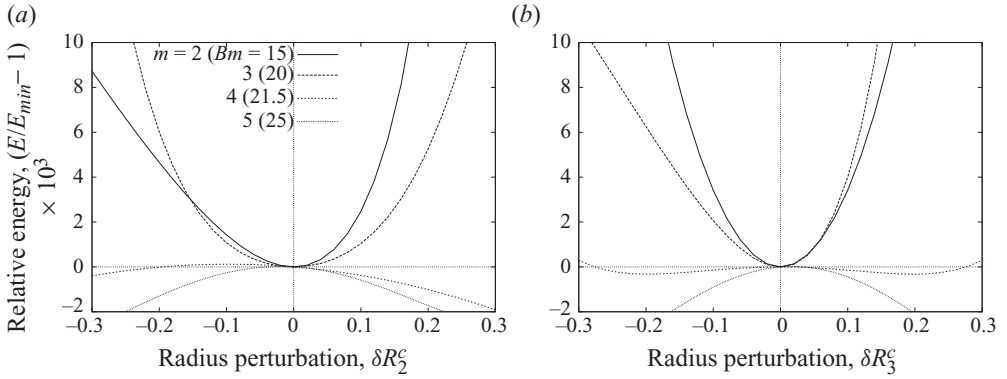

FIGURE 11. The associated energy normalised with its minimum for near equilibrium shapes of rotational symmetries with $m=2, 3, 4, 5$ versus the perturbation of the cosine amplitude of $m=2$ (a) and $m=3$ (b) modes defined by R_2^c and R_3^c coefficients in (4.2).

the associated electromagnetic problem was formulated in terms of a surface integral equation for the scalar magnetic potential. This equation was solved numerically on an unstructured triangular mesh covering the surface of the drop. Numerical method was validated against analytical solution for the stability of circular disk with respect to small-amplitude azimuthally harmonic edge perturbations. According to the analytical solution, the edge deformations with the azimuthal wavenumbers $m=2, 3, 4, \ldots$ start to grow on circular disk as the magnetic Bond number exceeds the critical threshold values $Bm_c^{(m)}=3\pi(m+1)/2$. The most unstable is $m=2$ mode, which corresponds to an elliptical deformation at the critical Bond number $Bm_c^{(2)}=9\pi/2\approx 14.1$.

This result agrees surprisingly well with the experimental findings of Conrath *et al.* (2006), Conrath (2007) for a drop of Galinstan (GaInSn eutectic alloy) with the diameter of $2R_0=65$ mm confined in a horizontal gap between two parallel glass plates separated by $h=3$ mm. The drop was submitted to the AC magnetic field generated by a 10-winding ($n=10$) coil with the inner and outer radii of $R_1=48$ mm and $R_2=81$ mm, respectively, which were roughly in the plane of the drop. For the

AC frequency of $f \approx 43\,\mathrm{kHz}$, which was the highest one applied in the experiment, an originally circular disk became elliptical as the effective current in the coil exceeded $I \approx 75\,\mathrm{A}$. This corresponds to the r.m.s. magnetic field in the centre of the coil

$$\frac{B_0}{\sqrt{2}} \approx \frac{\mu_0 n I}{2} \frac{\ln R_2 - \ln R_1}{R_2 - R_1} \approx 7.5\,\mathrm{mT}, \tag{5.1}$$

which yields the critical Bond number $Bm = B_0^2 R_0^2/\mu_0 \pi h \gamma \approx 14$, where $\gamma = 0.718\,\mathrm{N\,m^{-1}}$ is the surface tension of Galinstan and the effective arclength of the edge $l_0 \approx \pi h/2$ is approximated by a half circle. The critical currents are higher at lower frequencies and appear to saturate as the frequency is increased, which is consistent with the saturation of the electromagnetic force in the perfect conductor limit. Shapes with a rough threefold rotational symmetry are observed above the critical current $I \approx 100\,\mathrm{A}$, which corresponds to $Bm \approx 25$. This is by about a third greater than the theoretical value $Bm_c^{(3)} = 6\pi \approx 19$ for $m = 3$ mode. Note that also the shapes with a fourfold rotational symmetry are observed in the experiment though the numerical simulation showed them to be unstable. These discrepancies between the theory and experiment may be due to two effects. First, the size of the drop is comparable to that of the coil, which makes the applied magnetic field non-uniform over the drop radius. Second, to prevent the oxidation the drop is submerged in a 6 % solution of HCl, which may affect the surface tension. Given all these experimental uncertainties and deviations from the idealised theoretical model, the agreement of the instability threshold for the $m = 2$ mode seems too good and perhaps even incidental.

Note that the critical Bond number resulting from the energy variation approach is by a factor of 3 greater than that supplied by our previous linear stability analysis (Priede *et al.* 2006). There seem to be no obvious errors in either approach except for the factor of 2 missed in the final expression for the time-averaged force F_0 above equation (24) of Priede *et al.* (2006). This factor taken into account results in $Bm_c^{(m)} = \pi(m+1)/2$ which increases the actual difference from 1.5 to 3 times. The only questionable point is the determination of electromagnetic force on the edge, where the magnetic field becomes singular, by the integration of Maxwell stress tensor over a small cylindrical surface enclosing the edge (Priede *et al.* 2006). It is important to notice that the local magnetic field at the edge used in the integration is entirely due to the currents induced in the sheet. Using Ampere's force law, it can be shown that such an approach accounts only for the interaction between the induced currents while it misses out any interaction of the induced and external currents. This is because the latter act via the external magnetic field, which is opposite to the induced one, but not taken into account by the local field distribution. As a result, the force on the edge is overestimated and, consequently, the magnetic field strength necessary for the instability underestimated. Obviously, the semi-infinite sheet model used by Priede *et al.* (2006) is not able in principle to account for the interaction with external magnetic field, which requires the consideration of finite size system. This is implied also by the energy variation approach, which does not work for a semi-infinite sheet model. On the one hand, the energy of the magnetic field, which falls off as $\sim 1/\sqrt{r}$ from the edge, diverges for semi-infinite sheet. On the other hand, this energy does not vary with the variation of the edge position because this variation is equivalent to the offset of the origin of coordinate system. This makes the force on the edge of semi-infinite sheet undetermined. Such ambiguities do not arise when the energy variation approach is applied to finite-size drops, as done in this study. Moreover, difficulties due to the edge singularity disappear altogether when smooth drops are

considered, which, however, significantly increases the numerical complexity of the problem.

I would like to thank Y. Fautrelle for stimulating discussions.

Appendix. The magnetic potential for harmonically deformed disk

In the oblate spheroidal coordinates, (2.18) for the azimuthal mode m of the potential defined by (3.5) takes the form

$$\frac{\partial}{\partial\eta}\left((1-\eta^2)\frac{\partial\hat{\Psi}_1^m}{\partial\eta}\right)+\frac{\partial}{\partial\xi}\left((1+\xi^2)\frac{\partial\hat{\Psi}_1^m}{\partial\xi}\right)-\frac{m^2(\eta^2+\xi^2)}{(1-\eta^2)(1+\xi^2)}\hat{\Psi}_1^m=0. \tag{A 1}$$

The potential perturbation, which is supposed to vanish with the distance from the disk $\hat{\Psi}_1^m|_{\xi\to\infty}\to 0$, is related with the radius perturbation by (3.4), which now reads as

$$\hat{\Psi}_1^m\Big|_{r\to 1}=-\frac{2}{\pi\eta}\Big|_{\eta\to 0}. \tag{A 2}$$

Although (A 1) admits the variable separation, such a solution is complicated by the edge singularity (A 2). Nevertheless, a compact analytical solution can be found similarly to the construction of spherical solid harmonics from the fundamental solution of the Laplace equation (Batchelor 1973) as follows. Firstly, note that if Ψ is a solution of the Laplace equation and $\boldsymbol{\epsilon}$ is a constant vector, then $(\boldsymbol{\epsilon}\cdot\nabla)\Psi$ is a solution, too. Secondly, if Ψ satisfies a homogeneous boundary condition and $\boldsymbol{\epsilon}$ is directed along the boundary, then $(\boldsymbol{\epsilon}\cdot\nabla)\Psi$ satisfies that boundary condition, too. Thirdly, the operator $(\boldsymbol{\epsilon}\cdot\nabla)$ changes the radial dependence of Ψ from $\sim(r-1)^\alpha$ to $\sim(r-1)^{\alpha-1}$, while the azimuthal dependence is changed from the mode m to $m+1$. Algebra becomes particularly simple when $\boldsymbol{\epsilon}$ is taken in the complex form as $\boldsymbol{\epsilon}=\boldsymbol{e}_x+\mathrm{i}\boldsymbol{e}_y=\mathrm{e}^{\mathrm{i}\phi}(\boldsymbol{e}_r+\mathrm{i}\boldsymbol{e}_\phi)$. Then each application of $(\boldsymbol{\epsilon}\cdot\nabla)$ is accompanied by the multiplication with $\mathrm{e}^{\mathrm{i}\phi}$. Thus, the solution for $m=1$ is obtained straightforwardly from the axisymmetric base state (3.1) as

$$\hat{\Psi}_1^1(\eta,\xi)=-\mathrm{e}^{-\mathrm{i}\phi}\,(\boldsymbol{\epsilon}\cdot\nabla)\,\Psi_0=-\frac{\pi}{2}\left(\frac{1-\eta^2}{1+\xi^2}\right)^{1/2}\frac{\eta}{\eta^2+\xi^2}. \tag{A 3}$$

Higher azimuthal modes can be obtained similarly as $\hat{\Psi}_1^m=\mathrm{e}^{-\mathrm{i}m\phi}\,(\boldsymbol{\epsilon}\cdot\nabla)^m\,\hat{\Psi}_0^m$, where $\hat{\Psi}_0^m$ is an axisymmetric solution satisfying (A 1). The edge condition (A 2)

$$(\boldsymbol{\epsilon}\cdot\nabla)^m\,\Psi_0^m\sim\frac{\Psi_0^m}{\eta^{2m}}\sim\frac{1}{\eta} \tag{A 4}$$

yields $\Psi_0^m\sim\eta^{2m-1}$ for $\eta\to 0$. Moreover, the perturbation vanishes far away from the disk when $\hat{\Psi}_0^m|_{\xi=0}=c_0^m\eta^{2m-1}$ along the whole disk, where c_0^m is a constant. Then the corresponding axisymmetric solution of (A 1) can be written as

$$\Psi_0^m(\eta,\xi)=c_0^m\sum_{k=1}^{m}c_k^m P_{2k-1}(\eta)Q_{2k-1}(\mathrm{i}\xi), \tag{A 5}$$

where $P_n(x)$ and $Q_n(x)$ are the Legendre polynomials and functions of the second kind, respectively (Abramowitz & Stegun 1972); the expansion coefficients are found

as $c_k^m = (4k - 1/Q_{2k-1}(0))I_k^m$, where

$$I_k^m = \int_0^1 \eta^{2m-1} P_{2k-1}(\eta)\,\mathrm{d}\eta = \frac{\sqrt{\pi}2^{1-2m}(2m-1)!}{(m-k)!\Gamma(m+k+1/2)}. \tag{A 6}$$

Then the solution for the perturbation amplitude can be written as

$$\hat{\Psi}_1^m = D_{m-1}^+ D_{m-2}^+ \cdots D_1^+ D_0 \Psi_0^m, \tag{A 7}$$

using the operator

$$D_m^\pm \equiv \frac{r}{\eta^2 + \xi^2}\left(\xi\frac{\partial}{\partial\xi} - \eta\frac{\partial}{\partial\eta}\right) \pm \frac{m}{r}, \tag{A 8}$$

which is defined by $D_m^\pm \equiv \mathrm{e}^{-\mathrm{i}(m\pm1)\phi}\left(\boldsymbol{\epsilon}_\pm \cdot \nabla\right)\mathrm{e}^{\mathrm{i}m\phi}$, where $\boldsymbol{\epsilon}_+ = \boldsymbol{\epsilon}$, and $\boldsymbol{\epsilon}_- = \boldsymbol{\epsilon}^*$ is the complex conjugate of $\boldsymbol{\epsilon}$. The calculation of (A 7) is algebraically complicated but can be done by the computer algebra system Mathematica (Wolfram 1996), which requires considerable computer resources and practically can be carried out only for $m \leqslant 5$. But this suffices to deduce the general solution (3.6).

The axisymmetric solution (3.10) with $\sim\eta^{-3}$ edge singularity can be obtained in a similar way directly from the axisymmetric base solution (3.1) by applying $(\boldsymbol{\epsilon}_- \cdot \nabla)(\boldsymbol{\epsilon}_+ \cdot \nabla) \equiv D_1^- D_0^+$. This operator is equivalent to $-\partial_z^2$ because it represents the transversal part of the Laplace operator while (3.1) satisfies the Laplace equation.

REFERENCES

Abramowitz, A. & Stegun, I. A. 1972 *Handbook of Mathematical Functions*. Dover.

Baptiste, L., van Landschoot, N., Gleijm, G., Priede, J., Schade van Westrum, J., Velthuis, H. & Kim. T-Y. 2007 Electromagnetic levitation: A new technology for high rate physical vapour deposition of coatings onto metallic strip. *Surf. Coating Technol.* **202**, 1189–1193.

Batchelor, G. K. 1973 Three-dimensional flow fields extending to infinity. In *An Introduction to Fluid Dynamics*. sec. 2.9, p. 121. Cambridge.

Chandrasekhar, S. 1961 General variational principle. In *Hydrodynamic and Hydromagnetic Stability*, chap. 14. Oxford.

Conrath, M., Kocourek, V. & Karcher, Ch. 2006 Behavior of a liquid metal disc in a magnetic field of a circular current loop. In *Fifth International Symposium on Electromagnetic Processing of Materials (EPM 2006)*, Sendai, Japan, pp. 210–213.

Conrath, M. 2007 Dynamics of liquid metal drops influenced by electromagnetic fields. PhD Thesis, Ilmenau University of Technology, Germany, chap. 5, pp. 54–58.

Cowper, G. R. 1973 Gaussian quadrature formulas for triangles. *Intl J. Numer. Meth. Engng* **7**, 405–408.

Fautrelle, Y., Sneyd, A. & Etay, J. 2007 Effect of AC magnetic fields on free surfaces. In *Magnetohydrodynamics – Historical Evolution and Trends* (ed. S. Molokov, R. Moreau & H. K. Moffatt), pp. 345–355. Springer.

Hinaje, M., Vinsard, G. & Dufour, S. 2006*a* Determination of stable shapes of a thin liquid metal layer using a boundary integral method. *J. Phys.* D: *Appl. Phys.* **39**, 1244–1248.

Hinaje, M., Vinsard, G. & Dufour, S. 2006*b* Analytical modelling of a thin liquid metal layer submitted to an ac magnetic field. *J. Phys.* D: *Appl. Phys.* **39**, 2641–2646.

Kocourek, V., Karcher, Ch., Conrath, M. & Schulze, D. 2006 Stability of liquid metal drops affected by a high-frequency magnetic field. *Phys. Rev.* E **74**, 026303 (1–7).

Li, L.-W., Kang, X.-K. & Leong, M.-S. 2002 *Spheroidal Wave Functions in Electromagnetic Theory*, pp. 13–17. Wiley.

Mohring, J.-U., Karcher, C. & Schulze, D. 2005 Dynamic behavior of a liquid metal interface under the influence of a high-frequency magnetic field. *Phys. Rev.* E **71**, 047301 (1–4).

Perrier, D., Fautrelle, Y. & Etay, J. 2003 Free surface deformations of a liquid metal drop submitted to a middlefrequency AC magnetic field. In *Fourth International Conference on*

Electromagnetic Processing of Materials (EPM 2003), (ed. S. Asai, Y. Fautrelle, P. Gillon & F. Durand), Lyon, France, pp. 279–282.

Press, W. H., Teukolsky, S. A. & Vetterling, W. T. 1996 Directions set (Powell's) methods in multidimensions. In *Numerical Recipes in Fortran 90: The Art of Parallel Scientific Computing,* sec. 10.5.

Priede, J., Etay, J. & Fautrelle, Y. 2006 Edge pinch instability of liquid metal sheet in a transverse high-frequency ac magnetic field. *Phys. Rev.* E **73**, 066303 (1–10).

Sneyd, A. D. & Moffatt, H. K. 1982 Fluid dynamical aspects of the levitation melting. *J. Fluid Mech.* **117**, 45–70.

Wolfram, S. 1996 *The Mathematica Book*, 3rd edn. Wolfram Media.